In situ formation of TiB_2 nanoparticles for enhanced dehydrogenation/hydrogenation reaction kinetics of $LiBH_4$-MgH_2 as a reversible solid-state hydrogen storage system

Fahim Karimi[1,*], María Victoria Castro Riglos,[3] Julián Puszkiel,[1,2] Antonio Santoru,[1] Armin Hoell,[4] Chiara Milanese,[5] Nils Bergemann,[1] Claudio Pistidda, [1] Pau Nolis,[6] Maria D. Baro,[7] Gökhan Gizer,[1] Thi Lie Lu,[1] Klaus Pranzas,[1] Martin Dornheim,[1] Thomas Klassen[1] and Andreas Schreyer[8]

[1] Department of Nanotechnology, Institute of Materials Research, Helmholtz–Zentrum Geesthacht, Max-Planck-Straße 1, 21502 Geesthacht, Germany.

[2] Department of Physicochemistry of Materials, Consejo Nacional de Investigaciones Científicas y Técnicas (CONICET) and Centro Atómico Bariloche, Av. Bustillo km 9500 S.C. de Bariloche, Argentina.

[3] Department of Metalphysics, Consejo Nacional de Investigaciones Científicas y Técnicas (CONICET) and Centro Atómico Bariloche, Av. Bustillo km 9500 S.C. de Bariloche, Argentina.

[4] Institute for Nanospectroscopy, Helmholtz-Zentrum Berlin, Hahn-Meitner-Platz 1, 14109 Berlin, Germany.

[5] Pavia Hydrogen Lab, C.S.G.I. &Chemistry Department, Physical Chemistry Section, University of Pavia, Viale Taramelli, 16 , 27100 Pavia, Italy

[6] Servei de Ressonància Magnètica Nuclear, Universitat Autònoma de Barcelona, Cerdanyola del Vallès, Spain

[7] Departament de Física, Facultat de Ciències, Universitat Autònoma de Barcelona, E-08193 Bellaterra, Cerdanyola del Vallès, Barcelona, Spain

[8] European Spallation Source ERIC Box 176 S-22100 Lund, Sweden.

KEYWORDS: Hydrogen storage, Reactive hydride composites, structure analysis, nanoparticles

In order to enhance the de/rehydrogenation kinetic behavior of $LiBH_4$-MgH_2 composite system, TiF_4 is used as additive. The effect of this additive on the hydride composite system has been investigated by means of laboratory and advanced synchrotron techniques. Investigations on the synthesis and mechanism upon hydrogen interaction show that the addition of TiF4 to 2LiBH4-MgH2 during milling leads to the *in situ* formation of well distributed nanosized TiB2 particles. These TiB2 nanoparticles act as nucleation agents for the formation of MgB2 upon dehydrogenation process of $LiBH_4$-MgH_2 composite system. The effect of TiB2 nanoparticles are maintained upon cycling.

Introduction

Complex metal hydrides are considered as potential candidates for hydrogen storage materials for mobile applications[1,2]. They can provide an efficient and safe way to store hydrogen in comparison to hydrogen stored in gaseous or liquid state.3 Among all complex hydrides, $LiBH_4$ is widely investigated in past years[4-22]. This is due to its high hydrogen gravimetric and volumetric capacities, i.e. 18.4 wt. % and 121 kg/m3, respectively[23]. Nonetheless, the thermodynamic stability of $LiBH_4$ precludes the reversible reaction with hydrogen at moderate temperatures and pressures.[24] It releases hydrogen above its melting point (275 °C)[25] at temperatures between 480-490 °C through the reaction (1): $LiBH_4 \rightarrow B + LiH + 1.5H_2$, ΔH= 94 kJ/mol H_2 and its rehydrogenation occurs only above 650 °C and 15 MPa of hydrogen pressure.[4-6,24] Furthermore, highly toxic borane compounds can be formed during the dehydrogenation process of $LiBH_4$.[18] Many attempts have been taken to face the poor

reversibility and sluggish rehydrogenation kinetic of this system.[4-6,19-23] A breakthrough was achieved by the method of reactive hydride composite (RHC).[26,27] In this approach highly stable complex hydride such as $LiBH_4$ is mixed with a less stable binary hydride like MgH_2 (74 kJ/mol H_2) to lower the overall thermodynamic stability of the composite system.[26-40] The stoichiometric hydride composite system $2LiBH_4+MgH_2$ (Li-RCH) has a theoretical gravimetric capacity of 11.5 wt. % and a theoretical reaction enthalpy of 45.9 kJ/mol H_2, based on reaction (2): $2LiBH_4 + MgH_2 \leftrightarrows 2LiH + MgB_2 + 4H_2$. Thus, the overall thermodynamic stability of this system is reduced in comparison to reaction (1). This is mainly due to exothermal formation of MgB_2 during the desorption process. Therefore, MgB_2 is the key product for stabilization of $LiBH_4$ products upon its decomposition process. Experimentally, however, the dehydrogenation reaction of the Li-RHC system does not occur according to reaction (2). It rather decomposes in two reaction steps according to following reaction (3): $2LiBH_4 + MgH_2 \rightarrow Mg + 2LiBH_4 + H_2 \rightarrow 2LiH + MgB_2 + 4H_2$.[28] Furthermore, this reaction only occurs at hydrogen backpressures higher than 0.3 MPa and 400 °C. At hydrogen backpressures lower than 0.3 MPa, this composite system decomposes independently, and MgB_2 is not formed.[41,42] In recent years notable improvements of dehydrogenation/hydrogenation kinetic behaviour of RHCs have been achieved by addition of transition metals halides.[43-50]

In this work, the effect of TiF_4 as an additive in the Li-RHC is investigated. The addition of TiF_4 in the Li-RHC is motivated by the fact that titanium has the lowest atomic mass (relative to other transition metals) which leads to small loss of hydrogen storage capacity of the composite system. Moreover, TiF_4 showed significant dehydrogenation/hydrogenation enhancement kinetic in the Li-RHC system. Systematic, and extensive experimental investigations have been conducted in this work by the use of laboratory and advanced synchrotron techniques to shed some light on the reasons hidden behind the catalytic effect of TiF_4 in the Li-RHC system.

The results obtained in this work can contribute for fundamental understanding of the mechanism of nanosized transition metal borides and their effects in the Li-RHC system.

Experimental

$LiBH_4$ powder (purity > 90%), MgH_2 (purity > 95%), titanium fluoride (TiF_4, purity > 99.9 %) were purchased from Alfa Aesar company and used as starting materials. $2LiBH_4+MgH_2$ mixture were prepared with and without additive (TiF_4) by high energy ball milling in a SPEX 8000 mixer mill using a stainless steel vial and balls, respectively. The ball to powder ratio was chosen to be 10:1. In the first step MgH_2 was pre-milled for 5 hour. Subsequently, it was mixed with $2LiBH_4$ or $2LiBH_4 + 0.1TiF_4$, and the mixture was further milled for additional 5 hours. After milling the $2LiBH_4 + MgH_2 + 0.1TiF_4$, was subjected to a gas phase analysis. Therefore, a Hiden Analytical HAL 201 Mass-Spectrometer was used.

Hydrogen kinetic behaviors of the pure and doped sample were assessed in a commercial Sievert's type apparatus (PCTpro 2000). The parameters for volumetric measurements were set to 390 °C at 4 bar H_2 for desorption and 350 °C at 50 bar H_2 for absorption, respectively. First the materials in hydrogenated state were non-isothermally dehydrogenated with a temperature ramp set to 3 °C/min and then two hydrogenation-dehydrogenation cycles in isothermal conditions were preformed. Coupled calorimetric-volumetric measurements of the $2LiBH_4+MgH_2+0.1TiF_4$ composite system were performed by connecting a PCTPro instrument with a Sensys high-pressure DSC (Setaram, HP-DSC, France). The experimental parameters were: heating ramp 3 ºC/min, backpressure of 4 bar H_2 and final temperature of about 500 ºC.

Ex situ lab XRD were collected with a Bruker D8 Advance diffractometer in Bragg-Brentano geometry using a General Area detector and a Cu X-ray source. The sample was investigated using an airtight sample holder from Bruker. The incoherent scattering of the Poly (methyl methacrylate) dome is responsible for the bump observed at low angles in all the diffractograms.

In situ Synchron Radiation X-ray Powder Diffraction (*in situ* SR-XPD) measurements were conducted at the powder diffraction beamline D3 at HASYLAB (in DESY, Hamburg, Germany). Sample preparation was carried out in a glove box under inert conditions. A small amount of the specimen was charged in single crystal sapphire capillary. The capillary, subsequently, was mounted in a high-pressure cell and exposed to a monochromatic synchrotron beam. The wavelength of the incident photons was set to about 0.5 Å. The sample was heated up by a tungsten wire under the capillary while the sample temperature was measured by a thermocouple and controlled with a PID regulator. The diffracted intensities were collected by using a MarCCD-165 area detector. The acquired 2D-pattern were further processed and integrated to 1D-pattern using the program Fit2D.[51]

Anomalous small-angle scattering (ASAXS) measurements were acquired at the 7T-MPW beamline at the synchrotron radiation facility BESSY II (HZB, Berlin, Germany).[52] The beamline was equipped with a Si_{111} double crystal monochromator and a pair of retractable collimating/focusing mirrors optics leading to a resolution of $\Delta E/E \sim 2x10^{-4}$. A multi-wire proportional counter gas detector (20x20 cm^2, in size) was used to record the scattering data. All samples were put into a circular hole (5 mm in diameter) of an aluminum holder and sealed with Kapton tape to avoid any oxidation. Two sample-to-detector distances (SDD) ($D_{min.}$= 410 mm and $D_{max.}$= 1500 mm) were chosen in order to cover the maximum experimentally accessible scattering vector (q)-range. In order to separate the resonant scattering of Ti-containing nanostructures, all measurements were carried out close to the K absorption-edge of titanium (4966 eV).[56] All

selected energies with their corresponding anomalous dispersion factors are listed in Table 1.[57]

The raw data were processed using the software provided at the beamline. All SAXS measurements were integrated, than corrected for detector sensitivity and transmission. Measured intensities were than subtracted by dark current and background. For each measurement, a glassy carbon (with a thickness of 90 μm) and a silver-behenate foil was measured to put the scattering intensities onto absolute scales and to calibrate the *q*-axis, respectively. Furthermore, energy dependent inelastic scattering[59] at high *q*-values were subtracted by following the Porod-law. The resonant scattering of Ti-containing structures was separated using the method of Goerikg *et al.*[60]

Table 1. Selected energies for ASAXS-measurements at titanium K-edge (4966 eV), and the corresponding anomalous dispersion coefficients.

Element	Energy (eV)	*f'*	*f"*
E1	4600	-2.427	0.508
E2	4905	-4.214	0.454
E3	4955	-6.059	0.462
E4	4964	-7.798	0.587

XAS data were collected at the beamline A1 at HASYLAB (DESY, Hamburg, Germany). The samples were mixed with cellulose (~50 mg) in a mortar and mechanically pressed (with 5 bar) into pallets of 10 mm, in size. These pallets were than fixed in a circular hole of an aluminum sample holder and sealed with Kapton tapes (55 μm, in thickness) to avoid any oxidation of the samples. All XAS measurements were collected simultaneously in transmission and in fluorescence mode, respectively. XAS data processing and analyzing were carried out by using "IFEFFIT" software package.[61]

TEM characterization was performed in FEI TECNAI G^2 machine using 200 kV, point resolution: 0.12 nm and Field emission gun (FEG). Dark Field imaging technique (DF) was used to distinguish different phases by their diffraction. MgB_2 particles were highlighted by selecting one or more of the following MgB_2 phase´s intense reflections (hkl) planes: (101), having |g|=4.7 nm^{-1}, (002), having |g|=5.68 nm^{-1}, (110), having |g|=6.49 nm^{-1}. In the case of the additive (TiF_4), DF images were obtained by selecting the intense reflections from the following plane families: $(101)_{TiB2}$, having |g|=4.9 nm^{-1}, $(002)_{TiB2}$, having |g|=6.19 nm^{-1}. Size measurements on every particle were performed by means of an interpolated polygon tool from iTEM software[62] and the values that took into account were those from mean diameter measurements. High resolution transmission electron microscopy (HR-TEM) images were obtained with a magnification higher than M>300 Kx. In HR-TEM images Fast Fourier Transform (FFT) was performed by Digital Micrograph software[63] to obtain the diffraction patterns. Then the experimental diffraction patterns were compared with the simulated ones obtained by JEMS software[64]. Samples for TEM were prepared by dispersing a small amount of powder in hexane and then ultrasonicating the suspension during 10 min. A drop of this suspension was deposited over a commercial copper grid for TEM coated with a Formvar support film. The samples were exposed to the air during a short time.

^{11}B solid state NMR measurements were carried out on a Bruker Avance 400 MHz spectrometer with a wide bore 9.4 T magnet and employing a boron-free Bruker 4 mm CPMAS probe. The spectral frequency was 128.33 MHz for the ^{11}B nucleus, and the NMR shifts are reported in parts per million (ppm) externally referenced to BF_3Et_2O. The powder materials were packed into 4 mm ZrO_2 rotors in an argon-filled glovebox and were sealed with tight fitting Kel-F caps. The one-dimensional (1D) 11B{1H} MAS NMR spectra were acquired after a 2.7 μs single $\pi/2$ pulse (corresponding to a radio field strength of 92.6 kHz) and with application of a strong ^1H signal decoupling by using the two-pulse phase modulation (TPPM) scheme. The spectra were recorded at a MAS spinning rate of 12 kHz. Sample spinning was performed using dry nitrogen gas. The recovery delay was set to 10 s. Spectra were acquired at 20 °C (controlled by a BRUKER BCU unit).

All sample preparation, and handling were carried out in a glove-box under continuously purified argon atmosphere (H_2O and O_2 levels were kept below 10 ppm).

To determine the nature of the Ti containing species, thermodynamic calculations have been carried out using the HSC Chemistry software 9.4.1.[65] The calculations have been done based on the reactivity of the $2LiBH_4+MgH_2$ with TiF_4 under different temperature and pressure conditions. The most favorable reactions have been identified through a combination of Gibbs minimization equilibrium with selected solid and gas species. The obtained results represent ideal phase equilibrium compositions useful to predict possible reaction mechanisms between the Li-RHC matrix and the additive involving solid products and gaseous species such as B_2H_6, B_xH_y (x= 5 to 12, y = 5 to 14) and fluoride species. For all the calculations the solid orthorhombic $LiBH_4$ (*Pnma*) is taken into account. $Li_2B_{12}H_{12}$ was not taken into account owing to the lack of available physicochemical data.

Results

Volumetric and calorimetric measurements: Reaction kinetic

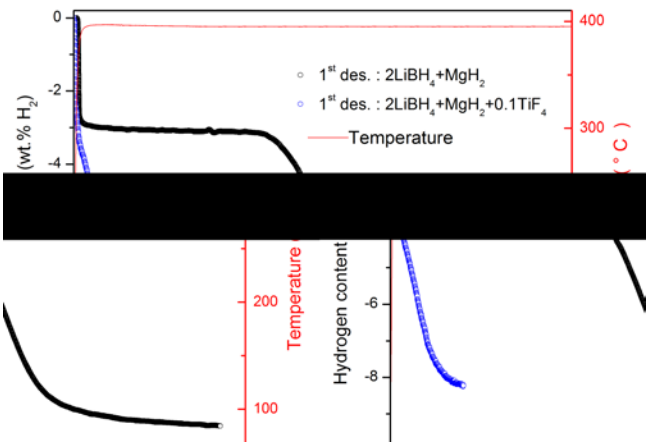

and reaction mechanism

The non-isothermal volumetric measurements of the pristine $2LiBH_4+MgH_2$ and $2LiBH_4+MgH_2+0.1TiF_4$ samples are presented in Fig. 1.

Figure 1. First non-isothermal dehydrogenation reaction from RT to 400 °C, heating rate 3 °C/min, and under PH_2= 4 bar H_2 dehydrogenation for $2LiBH_4+MgH_2$ and $2LiBH_4+MgH_2+0.1TiF_4$ hydride systems

The dehydrogenation reaction of pristine $2LiBH_4+MgH_2$ (Fig. 1) evolves roughly in 20 hours. The reaction proceeds in two steps separated by a plateau phase where hydrogen is almost not released. Subsequently, a plateau phase is built which extents for roughly about 6.5 hours. The second step of the reaction ends the plateau phase and it is completed after roughly 12 hours. The dehydrogenation processes of the $2LiBH_4+MgH_2+0.1TiF_4$ (Fig. 1) also shows two reaction steps. However, no plateau phase is observed and the overall reaction is completed in roughly after 2 hours. The kinetic behaviour of the first dehydrogenation is improved by adding 10 mol% of TiF_4 by a factor of ~ 5 relative to pure hydride system. Coupled calorimetric-volumetric measurements during the first dehydrogenation of $2LiBH_4+MgH_2+0.1TiF_4$ (ESI: Fig. S1) shows that from 50 ºC to about 360 ºC the material does not release hydrogen. However, the phase transition of $LiBH_4$ from orthorhombic to hexagonal structure as well as melting of the hexagonal structure are seen in the calorimetric signal at about 120 ºC and 270 ºC, respectively.[66,67] Neither the structural phase transition nor the melting point of $LiBH_4$ is affected by the presence of the used additive. The coupled calorimetric-volumetric measurements exhibit the same behaviour as the volumetric measurement for the $2LiBH_4+MgH_2+0.1TiF_4$ material (Fig. S1, and Fig. 1).

Furthermore, both materials were cycled twice and the results of the second cycle are shown in Fig. 2A and B. These volumetric measurements exhibit proper reversibility of the $2LiBH_4+MgH_2+0.1TiF_4$ system and still reduced hydrogenation (~ 1 h) and dehydrogenation (~ 2 h) times. Moreover, the hydrogen capacity remains constant in about 8 wt. % which is lower than the one of the pristine material because of the presence of the additive and a possible interaction between the $2LiBH_4+MgH_2$ matrix and the TiF_4 additive.

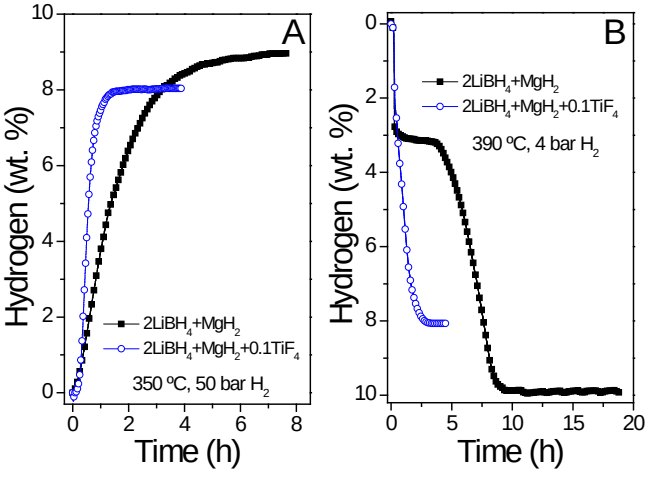

Figure 2. A) Second hydrogenation and **B)** Second dehydrogenation for $2LiBH_4+MgH_2$ and $2LiBH_4+MgH_2+0.1TiF_4$ hydride systems. Isothermal hydrogenation-dehydrogenation at 350 °C under 50 bar H_2 and 390 °C under 4 bar H_2, respectively.

***In situ* SR-XPD measurements: Phase transformation and reaction paths of Li-RHC**

By means of in situ SR-XPD, reaction paths of crystalline phases of $2LiBH_4+MgH_2+0.1TiF_4$ was investigated (Fig. 3). The starting material at room temperature consists of LiBH4, MgH_2, and LiF. By increasing the sample temperature, the diffraction peaks of the starting material become sharper and they are shifted slightly simultaneously toward lower diffraction angles. This is due to recrystallization of the disordered milled material and enlarging of the respective unit cells due to increased temperature, at the same time. Around 120 °C the phase transformation of $LiBH_4$ (from orthorhombic o-$LiBH_4$ to hexagonal h-$LiBH_4$) is observed. At 280 °C the diffraction peaks of $LiBH_4$ suddenly diminish, due to the melting of $LiBH_4$.[66,67] These findings are in good agreement with the results obtained by coupled calorimetric-volumetric measurements of the first dehydrogenation of the doped system. During the first reaction step MgH_2 decomposes around 360 °C by forming metallic Mg. In the second reaction step, at roughly 390 °C, the diffraction peaks of Mg decrease while diffraction peaks of MgB_2 phase start to appear. This indicates a mutual reaction between metallic Mg and the liquid $LiBH_4$. After dwelling for 30 min at 400 ºC (ESI: Fig. S2), LiF phase, and small amount of MgO phase are observed which remain stable. As the main reaction products LiH and MgB_2 are observed.

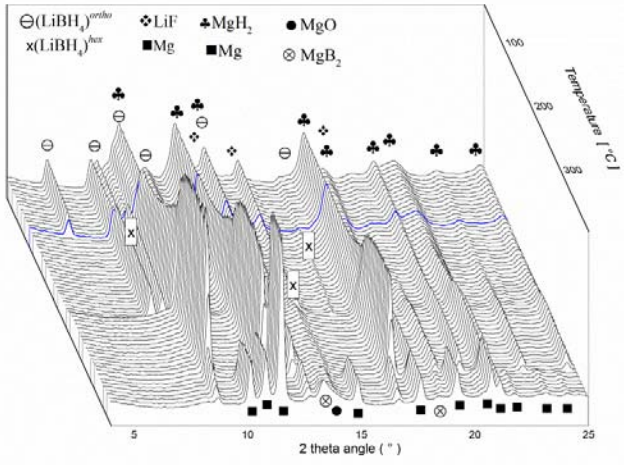

Figure 3. *In situ* SR-XRD for the first dehydrogenation reaction of $2LiBH_4+MgH_2+0.1TiF_4$ uder 4 bar H_2 back-pressure. The temperature was increased with a ramp of 3 °C/min from RT to a maximum temperature of 400 °C.

From the beginning, during the non-isothermal and isothermal *in situ* SP-XPD, no TiF_4 or any Ti containing phases could be detected (Fig.3 and Fig. S2). This suggests that Ti or any Ti containing compounds might be present in the

sample as an amorphous- or a nanocrystalline state. Therefore, X-ray Absorption Spectroscopy (XAS) measurements were carried out to determine the chemical state of Ti in the doped composite system. The great advantage of XAS technique is its insensitivity against the crystallinity or amorphous state of any given sample.

XAS measurements: Chemical state and local environment of titanium

Near Edge Structure (XANES) of the XAS-spectra of Ti in the $2LiBH_4+MgH_2+0.1TiF_4$ system at different hydrogenation state were extracted to determine the respective valance states of Ti (ESI: Fig. S3). TiF_4 and TiB_2 samples were measured as reference compounds. A comparison among TiF_4 spectrum, TiB_2 spectrum and the spectra of the $2LiBH_4+MgH_2+0.1TiF_4$ samples at different hydrogenation states reveals significant changes in the oxidation state of Ti in the hydride matrix. The oxidation state of Ti in the milled sample shows high dissimilarity to TiF_4 reference sample. This suggests a change in oxidation state of Ti already during the ball milling process. Thereafter, this oxidation state remains stable upon further de/rehydrogenation processes. On the other hand, the XANES spectra of the doped sample at different hydrogenation state have high similarity to the reference spectrum of TiB_2.

To further investigate the local environment of Ti atoms in the hydride matrix with respect to hydrogenation cycles, EXAFS ($\chi(k)$) region of the respective spectra were extracted and Fourier transformed. Fig. 4 displays the unweighted $\chi(k)$ (in the *k*-range from 0 Å to 6 Å) for the $2LiBH_4+MgH_2+0.1TiF_4$ samples together with reference spectra of TiF_4 and TiB_2.

The local environment of Ti in the $2LiBH_4+MgH_2$ composite system shows considerable changes after ball milling process. The shift in the position of the main amplitude of Ti spectra of the samples relative to TiF_4 spectrum hints to a removal of flour atoms and the presence of other species as the nearest neighborhood (NN). Moreover, substantial decrement of the amplitudes behind the principle amplitude around the central Ti atom is observed, which indicates a high degree of disorder/dispersion of Ti containing particles (nano sized). After first dehydrogenation, the principle EXAFS-amplitudes are increased and remain relatively stable upon further de/rehydrogenation processes. This hints to a higher degree of ordering and/or slight growing of Ti containing structures relative to the ball milled samples. Furthermore, a comparison between FT-EXAF-spectra and the reference spectrum of TiB_2 shows a well correspondence over the entire *R*-range indicating the presence of B as NN of the central Ti-atom.

To verify the formation of TiB_2 in the doped samples at different hydrogenation states, *ab initio* calculations were carried out using the FEFF6- program.[61] The results of these calculation together with the EXAFS spectra of the samples are presented in Fig. 5. In the calculation, the magnitudes of scattering amplitudes were not corrected for electron relaxation processes, since the existence of the TiB_2 phase was the center of interest. FEFF-calculations were performed assuming crystalline state of TiF_4 (Space Group PNMA; Cryst. Sys. Orthorhombic, ICSD #78737) and crystalline state of TiB_2 (Space Group P6/MMM; Cryst. Sys. Hexagonal, ICSD #30330).

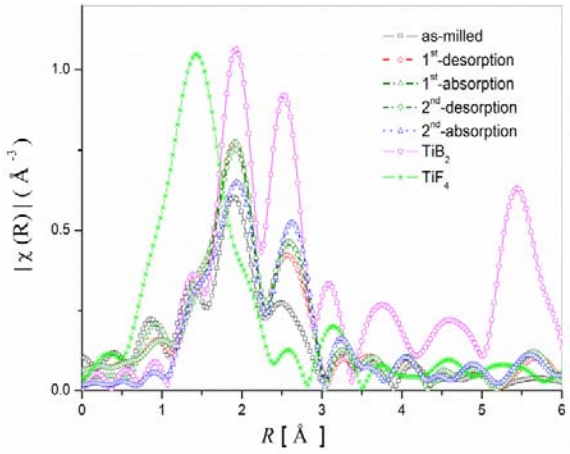

Figure 4. FT-transformation of the EXAFS-function in the *k*-range of [0-6] $Å^{-1}$ of Ti-containing hydride matrix at different hydrogenation cycles with the reference spectra.

The calculations allocated the first peak of TiF_4 to fluorine backscattering amplitude and the first and second peak of TiB_2 reference were addressed to boron and Ti backscattering amplitudes, respectively. This clarifies the transformation from TiF_4 to TiB_2 during the milling process of $2LiBH_4+MgH_2+0.1TiF_4$ material, which remains stable upon further de/rehydrogenation cycles. To determine the size distribution of TiB_2 particles in the hydride matrix ASAXS measurements were conducted.

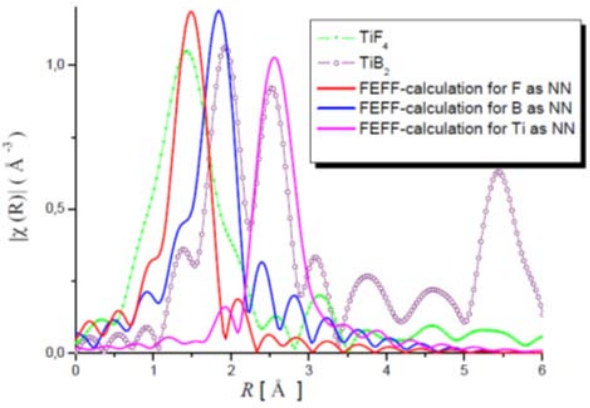

Figure 5. R-distribution-function of Ti-containing compounds in the hydride matrix after first hydrogenation cycle, and the corresponding FEFF-fits.

ASAXS measurements: Size distribution of TiB_2 particles

Anomalous Small-Angle X-ray Scattering (ASAXS) measurements, in the vicinity of titanium K-absorption edge, were carried out. The scattering intensities were collected at four pre-calculated X-ray energies (see Table 1, Experimental section) in order to separate the resonant scattering curves of Ti containing structures in the hydride matrix at different hydrogenation stages. In the ESI: Fig. S4 the ASAXS curves of as-milled $2LiBH_4+MgH_2+0.1TiF_4$ material are displayed. The anomalous scattering effect is clearly visible as the energy of incident beam increases (ESI: Fig. S4 - inset plot). At higher *q*-values a stronger energy dependency of scattering intensities is observed. This is due to fluorescence and resonant Raman scattering. This incoherent scattering causes a constant background at the very high *q*-values of the scattering curves, which was removed before analyzing the data. This was done by subtracting a constant value from all ASAXS-curves in such a manner so that the scattering curves at very high *q*-values follow the Porod-law.[68] Exemplarily, for all other curves, the resonant scattering curve of as-milled sample together with its corresponding total scattering and mixed resonant scattering curve are shown in ESI: Fig. S5. The resonant scattering curves were fitted by using the program Gnom.[69] Distance distribution functions of TiB_2 particles were calculated for all samples, assuming spherical particles. The results of these calculations are presented in Fig. 6. The maxima of the curves indicates the most frequent sizes of titanium containing structures in the samples, whereas the tail of the distance distribution function denotes the largest titanium containing structures.

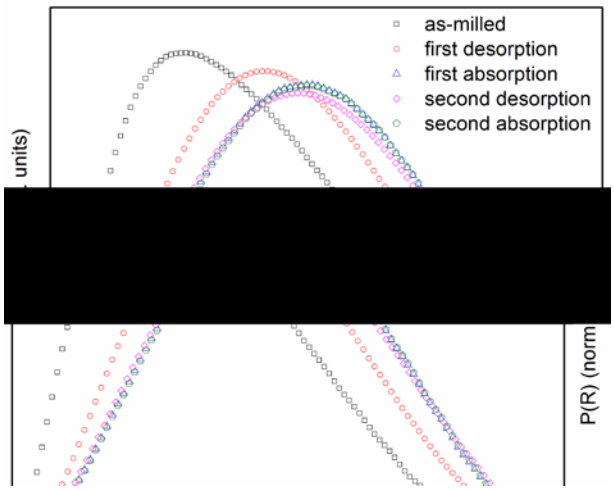

Figure 6. Distance-distribution curves of $2LiBH_4+MgH_2+0.1TiF_4$ material at different hydrogenation states.

In the as-milled $2LiBH_4+MgH_2+0.1TiF_4$ the most frequent TiB_2 particle sizes are about 7 nm which grow with the first dehydrogenation process up to ~ 13 nm. After the first absorption, a further growth of Ti-structures from 13 nm to approximately 16 nm is observed, which remains stable upon further re/dehydrogenation cycling. The largest structures in as-milled doped sample are about 27 nm which grow with the desorption process up to ~ 30 nm and remain relatively stable upon further cycling.

TEM observations: Morphological, nanoscopic structural and phase characterization

An electron diffraction pattern has been taken in order to find the most feasible phases (ESI: Fig. S6). The rings are correlated with the $d_{(hkl)}$ values taking into account the intensity of the rings. As seen, MgB_2 is detected, which is part of the matrix material. MgO is also present and its presence can be attributed to the short exposure of the sample to air during TEM preparation procedure which has not been possible to avoid. The LiF is detected, as well, as was shown by *in situ* SR-XPD measurements. Moreover, TiB_2 is clearly detected by the presence of a ring which can be only ascribed to TiB_2 phase. In Fig. 7, dark field (DF) TEM-images and particles size distributions of the $2LiBH_4+MgH_2$ (Fig. 7A) and $2LiBH_4+MgH_2+0.1TiF_4$ (Fig. 7B) after dehydrogenation are shown. It can be observed that the MgB_2 particles in the $2LiBH_4+MgH_2$ sample are in average about 100 nm in size, whereas, the average MgB_2 particles in the doped sample measure around 40 nm. Fig. 8 shows HR-TEM images in bright field (Fig. 8A, B and D) and in dark field (Fig. 8E) for the $2LiBH_4+MgH_2+0.1TiF_4$ material after the first dehydrogenation. Additionally, the Fourier transform from a particle (Fig. 8B) and the corresponding simulation along with the particle size distribution are exhibited (Fig. 8C and F). From the HR-TEM images it is possible to verify the presence of small particles of TiB_2 in the $2LiBH_4+MgH_2+0.1TiF_4$ after the first dehydrogenation. FT analysis (Fig. 8C) is in agreement with the electron pattern simulation, thus confirming that TiB_2 particles are formed. This result is in accordance with the XAS analysis. From DF image, size measurements have been carried out on numerous particles leading to a quite reliable size distribution. The TiB_2 shows reduced sizes compared to those from MgB_2 particles. As it is observed the average particle size from TiB_2 is about 16 nm with a range between 4 nm and 66 nm. This TiB_2 nano sizes are in good agreement with the ASAXS results (Fig. 6).

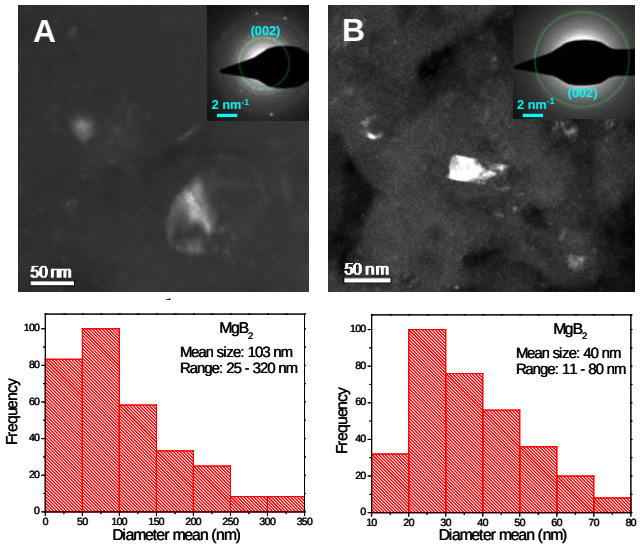

Figure 7. TEM in Dark field (DF) modus (top) and MgB_2 particle size distribution (bottom) in: $2LiBH_4+MgH_2$ (left) and $2LiBH_4+MgH_2+0.1TiF_4$ (right).

Discussion

The addition of TiF_4 significantly improves the dehydrogenation/hydrogenation kinetics of the $2LiBH_4+MgH_2$ composite system (Fig. 1 and ESI Fig. S1). During the first non-isothermal dehydrogenation the presence of TiF_4 precludes the long plateau period. This plateau phase is observed in the pristine Li-RHC system which proceeds with almost no hydrogen release. It has been reported before that this plateau phase might accounted for a slow incubation period required for the nucleation of MgB_2 seeds[43]. However, based on experimental evidence, it has been recently found that the plateau phase during the first dehydrogenation of the Li-RHC system is due to the slow formation of small amount of $Li_2B_{12}H_{12}$ from $LiBH_4$ according to the reaction: $2LiBH_4 \rightarrow (1/6)Li_2B_{12}H_{12} + (5/3)LiH + (13/6)H_2$.[70-72]. The formation of $Li_2B_{12}H_{12}$ partially blocks the interaction between $LiBH_4$ and Mg and the formation of MgB_2 is delayed. Moreover, the formation of gaseous B_2H_6, which further interacts with $LiBH_4$, can lead to formation of $Li_2B_{12}H_{12}$. However, the presence of backpressure during dehydrogenation can kinetically avoid formation of gaseous diborane (B_2H_6) as intermediate.[73-75] To shed light on the nature of the plateau region, TiB_2 powder has been ball milled for 10 hours. Subsequently, $0.1TiB_2$ (premilled powder) has been added to MgH_2 which has been already milled for 5 hours. Thereafter, $2LiBH_4$ has been added in the mixture and the entire composite system ($2LiBH_4+MgH_2+0.1TiB_2$) has been further milled for additional 5 hours.

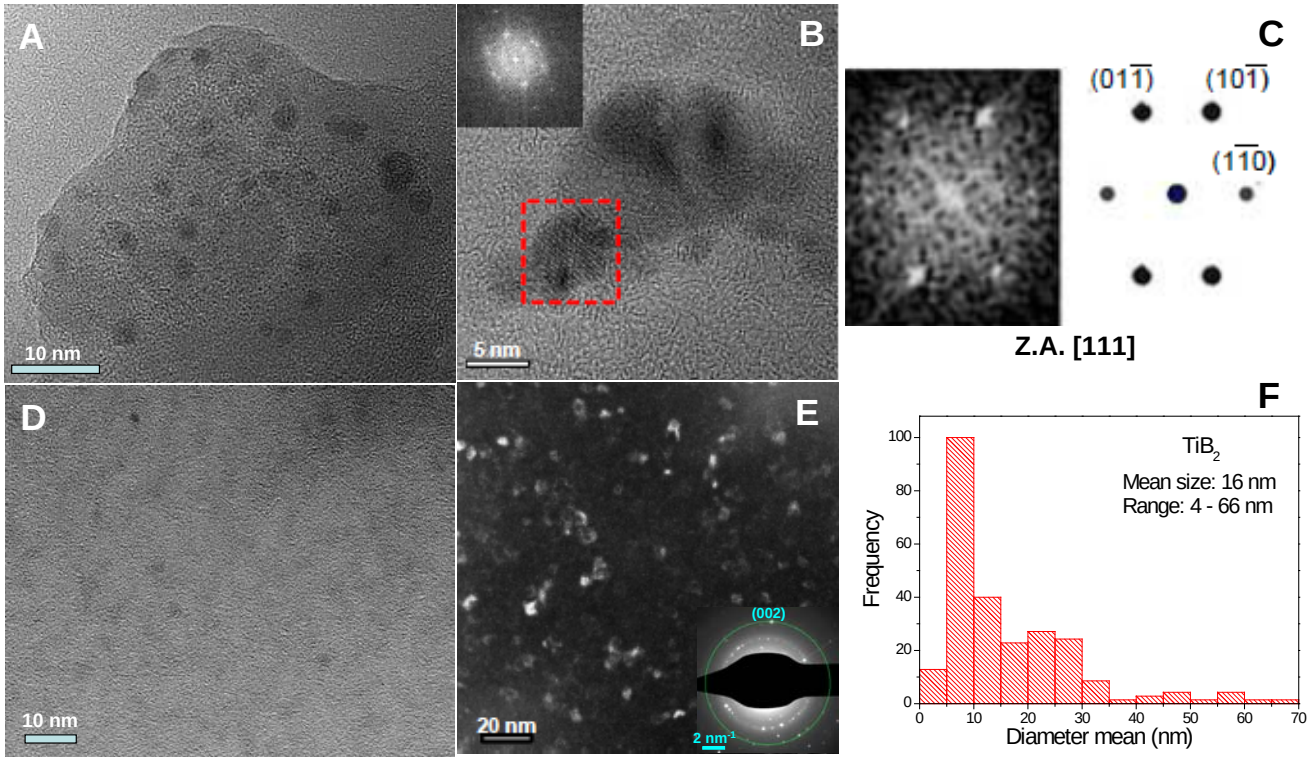

Figure 8. $2LiBH_4+MgH_2+0.1TiF_4$ after the first dehydrogenation: **A** and **B** HR-TEM images. **C** FT and structure simulation. **D** Bright field. **E** Dark field in the shown bright field region and inset plot of the diffraction used for the DF. **F** Particle size distribution of TiB_2.

The dehydrogenation kinetic of the $2LiBH_4+MgH_2+0.1TiB_2$ system has been measured by means of volumetric method. The results show (ESI Fig. S10.) that the plateau phase is significantly reduced by the presence of as-milled TiB_2. However, the plateau region does not disappear completely. Therefore, it is possible to infer that there must be some formation of $Li_2B_{12}H_{12}$ coming from the initial $LiBH_4$ decomposition and the amorphous boron in the starting material (ESI: Fig.S8). Despite this fact, the presence of TiB_2 provides more centres for the nucleation of MgB_2 promoting the early contact between $LiBH_4$ and Mg and thus partially avoiding the delay for the MgB_2 formation owing to the $Li_2B_{12}H_{12}$ barrier. For the case of $2LiBH_4+MgH_2+0.1TiF_4$, the nature of the *in situ* formed nanoparticles of TiB_2 is more effective because the plateau region is totally suppressed (Fig. 1 and Fig. S10). This can be ascribed to the nanosize of TiB_2 and the better distribution of nucleation centres for MgB_2. These experimental results and analyses allow inferring that the formation of $Li_2B_{12}H_{12}$ and the nucleation of MgB_2 seeds are two competing reactions upon the decomposition of $LiBH_4$ in the Li-RHC. Upon cycling, it is noticed that the presence of the additive causes a drop of the hydrogen capacity from about 10 wt. % H_2 to 8 wt. % H_2 in comparison to the pristine $2LiBH_4+MgH_2$ (Fig. 2). Nevertheless, the enhanced kinetic behaviour and hydrogen capacity of 8 wt. % remain stable.

In previous works, it has been found that the interaction of $3LiBH_4$:$1TiF_3$ stoichiometric mixture during milling leads to formation of volatile $Ti(BH_4)_3$.[76,77] Kang *et al.*[78] have shown the formation of nanosized TiB_2 by the interaction between $LiBH_4$ and TiF_3. They have found that a one step milling process leads to a partial formation of TiB_2. However, a three step method starting with a $1LiBH_4$:$0.04TiF_3$ stoichiometric mixture provides the full conversion to nanosized TiB_2. In this work, a one step milling procedure provides the full conversion to nanosized TiB_2 (Fig. 4, 5 and 8) from the interaction between the $2LiBH_4+MgH_2$ material and $0.1TiF_4$ additive.

To understand the interactions between the $2LiBH_4+MgH_2$ composite material and TiF_4, phase composition equilibrium calculations based on the Gibbs free energy minimization have been carried out with the HSC Chemistry software.[65] The calculations under different conditions such as mechanical milling, first dehydrogenation and first hydrogenation have been performed (ESI: Table S1). The equilibrium calculations predict that after milling the formation of LiF, TiB_2 and B is thermodynamically favoured according to the reaction (4): $0.4LiBH_4 + 0.1TiF_4 \rightarrow 0.4LiF + 0.1TiB_2 + 0.2B + 0.8H_{2(g)}$ (ΔG_{298K}= -57.2 kJ).

In situ SR-XRD shows the presence of LiF after milling (Fig. 3). Moreover, after milling the crystallite size of MgH2 in the $2LiBH_4+MgH_2+0.1TiF_4$ is further refined down to 8 nm in comparison with 15 nm for $2LiBH_4+MgH_2$ (ESI: Fig. S7 *Ex situ* XRD). NMR results (ESI: Fig. S8) evidence the presence of amorphous boron and boride compounds in as-purchased $LiBH_4$. For the as-milled $2LiBH_4+MgH_2+0.1TiF_4$ the amount of amorphous boron increases. MS measurement shows the presence of hydrogen in the milling chamber atmosphere (ESI: Fig. S9). These results are in accordance with the proposed reaction (4). Upon dehydrogenation and hydrogenation, the experimental results (Fig. 3, 4, 5 and 8) and the equilibrium thermodynamic calculation show that LiF and TiB_2 remain stable, under the applied conditions. This explains the reduction of hydrogen storage capacity of the $2LiBH_4+MgH_2+0.1TiF_4$ composite system in comparison to the pure Li-RHC. Furthermore, size distribution of TiB_2 has been determined *via* ASAXS measurements and TEM observations (Fig. 6 and 8). Both methods show roughly a size distribution of TiB_2 nano particles of around 10-16 nm. These TiB_2 nano particles are most likely responsible for the heterogeneous nucleation and growth of MgB_2 phase during the dehydrogenation of $2LiBH_4$-Mg. Calculations, carried out based on mismatch theory[78] have revealed two possible crystallographic matching planes between TiB_2 and MgB_2 ($MgB_2\{1010\}//TiB_2\{1010\}$=1.9 and $MgB_2\{1011\}//TiB_2\{1011\}$=4.5). These mismatch values are lower than 6 %, which is considered as the upper limit value.[79] Therefore, TiB_2 can provide two possible crystallographic nucleation planes for MgB_2. This assumption is further indirectly verified by the results obtained via TEM observation of MgB_2 particle size distribution in the matrix of pure and doped composite system (Fig. 7). In the doped system, the average MgB_2 particle size is about 40 nm and the maximum observed MgB_2 particle range is roughly 80 nm, whereas in the pure material the corresponding average size is about 100 nm and the maximum one is around 300 nm. This observation can be explained by assuming uniformly distributed TiB_2 nano particles in the hydride matrix which act as nucleation centres for MgB_2 phase during the dehydrogenation. Thus, MgB_2 seeds start to nucleate and grow around these nuclei. Due to vast number of these nucleation centres, which are uniformly distributed in material with additive, the nucleation of MgB_2 starts to take place in numerous places in the interface of LiBH4/Mg. This mechanism, indeed, leads to notably faster reaction kinetics and significantly smaller MgB_2 structures, in comparison to the corresponding pure Li-RHC system.

Conclusion

One step *in situ* synthesis of nanosized TiB_2 from the interaction between $LiBH_4$ and TiF_4 is observed which improves the dehydrogenation/hydrogenation rates of the $2LiBH_4+MgH_2$ composite system. The presence of nanosized TiB_2 notably reduces the dehydrogenation and hydrogenation times from 10-20 hours to less than 3 hours and from 8 h to about 1 h, respectively. Moreover, the Li-RHC system doped with $0.1TiF_4$ shows reversible hydrogen capacity of 8 wt. %. Furthermore, the chemical state of TiF_4 is changed. During the

ball milling procedure nanosized TiB_2 is formed which remains stable upon dehydrogenation/hydrogenation cycling. The observed kinetic improvement of the doped system could be inferred on its refined microstructure, homogenous distribution of nanosized TiB_2 and the feasibility TiB_2 to act as nucleation interfase for MgB_2.

ASSOCIATED CONTENT

Supposting information: Fig. S1 to S10 and Table S1.

ACKNOWLEDGMENT

The authors thank CONICET (Consejo Nacional de Invetigaciones Científicas y Técnicas), ANPCyT – (Agencia Nacional de Promoción Científica y Tecnológica), CNEA (Comisión Nacional de Energía Atómica), for financial support to carry out this work. We would also like to thank the Metals Physics Division for the TEM devices. The researchers leading to these results have received funding from the European Marie Curie Actions under ECOSTORE grant agreement no. 607040.

References

(1) Züttel, A., Borgschule, A. Schlapbach, L. Weinheim.; WILEY-VCH, Ed. 2008.

(2) Schlapbach, L.; Zuttel, A. *Nature* **2001**, *414*, 353.

(3) Schuth, F.; Bogdanovic, B.; Felderhoff, M. *Chemical Communications* **2004**, *0*, 2249.

(4) Züttel A., Wenger P., Rentsch S., Sudan P., Mauron Ph., Emmenegger Ch., Journal of Power Sources 118 (2003) 1–7.

(5) Züttel A., Rentsch S., Fischer P., Wenger P., Sudan P., Mauron P., *et al.*, J Alloy Compd. 2003;356-357:515-20.

(6) Orimo S., Nakamori Y., Ohba N., Miwa K., Aoki M., Towata S., Züttel A., Appl. Phys. Lett. 2006, 89, 021920.

(7) Ohba N., Miwa K., Aoki M., Noritake T., Towata S.I., Nakamori Y., *et al.*, Physical Review B - Condensed Matter and Materials Physics. 2006;74.

(8) Au M., Jurgensen A., Zeigler K., J. Phys. Chem. B 2006, 110:26482-26487.

(9) Kang X-D., Wang P., Ma L-P., Cheng H-M., Applied Physics A. 2007;89:963-6.

(10) Hwang S. J., Bowman R. C., Reiter J. W., Rijssenbeek J., Soloveichik G. L., *et al.*, J. Phys. Chem. C 2008, 112, 3164–3169.

(11) Zhang Y., Zhang W-S., Fan M-Q., Liu S-S., Chu H-L., Zhang Y-H., *et al.*, The Journal of Physical Chemistry C. 2008;112:4005-10.

(12) Mosegaard L., Møller B., Jørgensen J-E., Filinchuk Y., Cerenius Y., Hanson J.C., et al. The Journal of Physical Chemistry C 2008;112:1299-303.

(13) Au M., Jurgensen A.R., Spencer W.A., Anton D.L., Pinkerton F.E., Hwang S-J., et al.,The Journal of Physical Chemistry C. 2008;112:18661-71.

(14) Xu J., Yu X., Zou Z., Li Z., Wu Z., Akins D.L., *et al.*, Chemical Communications. 2008:5740-2.

(15) Fang Z-Z., Kang X-D., Wang P., Cheng H-M., The Journal of Physical Chemistry C. 2008;112:17023-9.

(16) Xia G.L., Guo Y.H., Wu Z., Yu X.B., J Alloy Compd. 2009;479:545-8.

(17) R. Caputo and A. Züttel, Molecular Physics, 2010, 108, 1263-1276.

(18) Friedrichs O., Remhof A., Hwang S.J., Züttel A., Chemistry of Materials. 2010;22:3265-8.

(19) Ngene P., van Zwienen M., de Jongh P.E., Chemical Communications. 2010;46:8201-3.

(20) Rude .LH., Groppo E., Arnbjerg L.M., Ravnsbæk D.B., Malmkjær R.A., Filinchuk Y., et al., J Alloy Compd. 2011;509:8299-305.

(21) Zavorotynska O., Corno M., Pinatel E., Rude L.H., Ugliengo P., Jensen T.R., et al., Crystals. 2012;2:144.

(22) Shao J., Xiao X., Fan X., Zhang L., Li S., Ge H., *et al.*, The Journal of Physical Chemistry C. 2014;118:11252-60.

(23) Orimo S-i., Nakamori Y., Eliseo J.R., Züttel A., Jensen C.M., Chem. Rev. 2007, 107, 4111-4132.

(24) P. Mauron, F. Buchter, O.Friedrichs, A. Remhof, M. Bielmann and C. N. Zwicky, *et al.*, J. Phys. Chem. B, 2008, 112, 906.

(25) Fedneva E.M., Alpatova V.L., Mikheeva V.I., Transl. of Zh. Neorg. Khim. Russ. J. Inorg. Chem. 1964; 9(6): 826–827.

(26) G. Barkhordarian, T. Klassen, R. Bormann, Patent, German Pub. No: DE1022004/061286 (2004).

(27) J.J. Vajo, S.L. Skeith, F. Mertens, J. Phys. Chem. B 109 (2005) 3719–3722.

(28) U. Bösenberg, S. Doppiu, L. Mosegaard, G. Barkohrdarian, et al., Acta Mater 55 (2007) 3951–3958.

(29) Mao J.F., Yu X.B., Guo Z.P., Liu H.K., WuZ., Ni J., J. Alloys Compd. 2009, 479, 619–623.

(30) Garroni S., Pistidda C., Brunelli M., Vaughan G.B.M., Suriñach S., Baró M.D., Scripta Materialia 2009, 60:1129–1132.

(31) Garroni S., Milanese C., Girella A., Marini A., Mulas G., Menéndez E., et al., International Journal of Hydrogen Energy. 2010;35:5434-41.

(32) Bonatto Minella C., Garroni S., Olid D., Teixidor F., Pistidda C., Lindemann I., *et al.* J Phys Chem C. 2011;115:18010-4.

(33) Karimi F., Klaus Pranzas P., Pistidda C., Puszkiel J.A., Milanese C., Vainio U., *et al.*, Physical Chemistry Chemical Physics. 2015;17:27328-42.

(34) Karimi F., Pranzas P.K., Hoell A., Vainio U., Welter E., Raghuwanshi V.S., *et al.*,Journal of Applied Crystallography. 2014;47:67-75.

(35) Minella C.B., Pistidda C., Garroni S., Nolis P., Baró M.D., Gutfleisch O., *et al.*, The Journal of Physical Chemistry C. 2013;117:3846-52.

(36) Vajo J.J., Li W., Liu P., Chem. Commun 2010; 46:6687-6689.

(37) Garroni S., Milanese C., Girella A., Marini A., Mulas G., Menéndez E., et al., International Journal of Hydrogen Energy. 2010;35:5434-41.

(38) Li G.Q., Matsuo M., Deledda S., Hauback B.C., Orimo S., Mater. Trans. 2014; 55: 1141–1143.

(39) Afonso G., Bonakdarpour A., Wilkinson D.P., J. Phys. Chem. C 2013; 117:21105–21111.

(40) Bergemann N., Pistidda C., Milanese C., Emmler T., Karimi F., Chaudhary A-L., *et al.*, Chemical Communications. 2016;52:4836-9.

(41) F. E. Pinkerton, M. S. Meyer, G. P. Meisner, M. P. Balogh and J. J. Vajo, J. Phys. Chem. C, 2007, 111, 12881.

(42) U. Bösenberg, D. B. Ravnsbæk, H. Hagemann, V. D'Anna, C. Bonatto Minella and C. Pistidda, et al., J. Phys. Chem. C, 2010, 114, 15212.

(43) U. Bösenberg, J.W. Kim, D. Gosslar, N. Eigen, T.R. Jensen and J.M. Bellosta von Colbe, et al., Acta Mater., 2010, 58, 3381.

(44) J.A. Puszkiel, F.C. Gennari, P. Arneodo Larochette, J.M. Ramallo-López, U. Vainio and F. Karimi, et al., J. of Power Sources, 2015, 284, 606.

(45) T. Sun, H. Wang, Q. G. Zhang, D. L. Sun, X. D. Yao and M. Zhu, J. Mater. Chem., 2011, 21, 9179.

(46)J. F. Mao, Z. P. Guo, X. B. Yu and H. K. Liu, J. Mater. Res., 2011, 26, 1143.

(47) E. Deprez, A. Justo, T. C. Rojas, C. Lopez-Cartes, C. B. Minella and U. Bösenberg, et al., Acta Mater., 2010, 58, 5683.

(48) E. Deprez, M. A. Muñoz-Márquez, M. C. Jimenez de Haro, F. J. Palomares, F. Soria, M. Dornheim, R. Bormann and A. Fernández, JOURNAL OF APPLIED PHYSICS 109, 014913, 2011.

(49) H. Q. Kou, X. Z. Xiao, J. X. Li, S. Q. Li, H. W. Ge and Q. D. Wang, et al., Int. J. Hydrogen Energy, 2012, 37, 1021–1026.

(50) X. Z. Xiao, J. Shao, L. X. Chen, H. Q. Kou, X. L. Fan and S. S. Deng, et al., Int. J. Hydrogen Energy, 2012, 37, 13147.

(51) A. P. Hammersley, FIT2D: An Introduction and Overview, ESRF Internal Report, ESRF97HA02T, FIT2D: An Introduction and Overview, 1997.

(52) M. Krumrey, J. Synchrotron Rad., 1998, 5, 6.

(53) H. Bieder, A. Hoell, L. Mokrani and I. Zizak, Patent DE102006029449. 2007.

(54) M. Krumrey, G. Ulm, Nucl. Instr. and Meth. A, 2001, 467–468, 1175.

(55) J. Wernecke, C. Gollwitzer, P. Müller and M. Krumrey, J. Synch. Rad., 2014, 21, 529.

(56) A. Hoell, D. Tatchev, S. Haas, J. Haug and P. Boesecke, J. Appl. Cryst., 2009, 42, 323.

(57) D. T. Cromer, D. Libermn, J. Chem. Phys., 1970, 53, 1891.

(59) U. Vainio, Neutrons and Synchrotron Radiation in Engineering Materials Science: From Fundamentals to Applications: Second Edition, Wiley, 2017, 217-225.

(60) G. Goerigk, K. Huber and R. Schweins, J. Chem. Phys., 2007, 127, 154908.

(61) B. Ravel and M. Newville, J. Synchrotron Rad., 2005, 12 (4), 537.

(62) i-TEM (License № A2382500).

(63) Digital Micrograph (License № 90294175).

(64) JEMs (License № IEb59yBDflUMh).

(65) Outokumpu HSC Chemistry for Windows, version 9.4.1, Outotec.

(66)E.M. Fedneva, V.L. Alpatova, V.I. Mikheeva, Transl. Zh. Neorg. Khim. Russ. J. Inorg. Chem. 9 (6) (1964) 826-827.

(67) T. Nakagawa, T. Ichikawa, H. Hanada, Y. Kojima, H. Fujii, J. Alloys Compd. 446-447 (2007) 306-309.

(68) G. Porod, Kolloid Z. 1951, 124, 83

(69) Svergun D and Semenyuk A 2003 PROGRAM PACKAGE GNOM http://www.embl-hamburg.de/ExternalInfo/ Research/Sax/

(70) Y. Yan, H.-W. Li, H. Maekawa, K. Miwa, S. Towata and S. Orimo, J. Phys. Chem. C, 2011, 115, 19419.

(71)K.-B. Kim, J.-H. Shim, S.-H. Park, I.-S. Choi, K. H. Oh and Y. W. Cho, J. Phys. Chem. C, 2015, 119, 9714.

(72) J. Puszkiel, M.V. Castro Riglos, F. Karimi, A. Santoru, C. Pistidda, T. Klassen, J. Bellosta von Colbe and M. Dornheim. Physical Chemistry Chemical Physics 2017, 19, 7455-7460.

(73)K.-B. Kim, J.-H. Shim, K. H. Oh and Y. Cho, Chem. Commun.,2011, 47, 9831.

(74) J. Kostka, W. Lohstroh, M. Fichtner and H. Hahn, J. Phys. Chem. C, 2007, 111, 14026.

(75) O. Friedrichs, A. Remhof, S.-J. Hwang and A. Zu¨ttel, Chem.Mater., 2010, 22, 3265.

(76) Fang ZZ, Ma LP, Kang XD, Wang PJ, Wang P, Cheng HM. Applied Physics Letters. 2009;94:044104.

(77)Callini E, Szilagyi PA, Paskevicius M, Stadie NP, Rehault J, Buckley CE, *et al.*, Chemical Science. 2016;7:666-72.

(78) X. Kang, K. Wang, Y. Zhong, B. Yang and P. Wang, hys.Chem. Chem. Phys., 2013, 15, 2153.

(79) M.-X. Zhang, P.M. Kelly, Scripta Mater. 52 (2005) 963–968.